

Learning Photometric Feature Transform for Free-form Object Scan

XIANG FENG, State Key Lab of CAD&CG, Zhejiang University, China
 KAIZHANG KANG, State Key Lab of CAD&CG, Zhejiang University, China
 FAN PEI, State Key Lab of CAD&CG, Zhejiang University, China
 HUAKENG DING, State Key Lab of CAD&CG, Zhejiang University, China
 JINJIANG YOU, State Key Lab of CAD&CG, Zhejiang University, China
 PING TAN, Hong Kong University of Science and Technology, China
 KUN ZHOU, State Key Lab of CAD&CG, Zhejiang University, China
 HONGZHI WU*, State Key Lab of CAD&CG, Zhejiang University, China

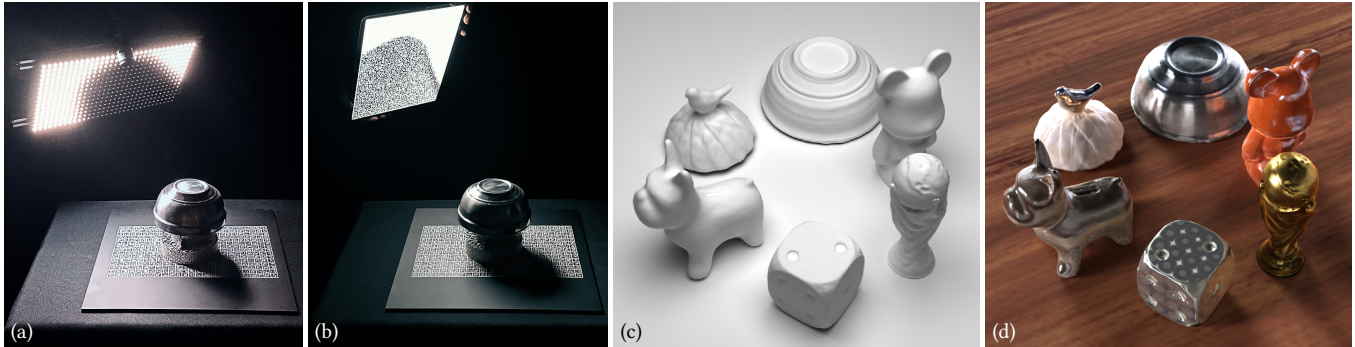


Fig. 1. Using an illumination-multiplexing device, such as a lightweight prototype consisting of a single camera and a programmable light array (a) or an off-the-shelf tablet (b), we propose a system that learns to acquire with pre-optimized time-varying lighting patterns at unstructured views, and reconstruct both the geometry (c) and complex anisotropic reflectance (d) of a number of challenging objects. Please refer to the accompanying video for animated rendering results.

We propose a novel framework to automatically learn to aggregate and transform photometric measurements from multiple unstructured views into spatially distinctive and view-invariant low-level features, which are fed to a multi-view stereo method to enhance 3D reconstruction. The illumination conditions during acquisition and the feature transform are jointly trained on a large amount of synthetic data. We further build a system to reconstruct the geometry and anisotropic reflectance of a variety of challenging objects from hand-held scans. The effectiveness of the system is demonstrated with a lightweight prototype, consisting of a camera and an array of LEDs, as well as an off-the-shelf tablet. Our results are validated against reconstructions

from a professional 3D scanner and photographs, and compare favorably with state-of-the-art techniques.

CCS Concepts: • **Computing methodologies** → **3D imaging; Shape modeling.**

Additional Key Words and Phrases: low-level features, feature learning, computational illumination, multi-view stereo

ACM Reference Format:

Xiang Feng, Kaizhang Kang, Fan Pei, Huakeng Ding, Jinjiang You, Ping Tan, Kun Zhou, and Hongzhi Wu. 2023. Learning Photometric Feature Transform for Free-form Object Scan. *ACM Trans. Graph.* 1, 1 (August 2023), 11 pages. <https://doi.org/10.1145/nnnnnnn.nnnnnnn>

1 INTRODUCTION

Free-form scanning of 3D geometry in the presence of complex appearance is an important problem in computer graphics and computer vision. It is useful for various applications including e-commerce, visual effects, 3D printing and cultural heritage.

This problem remains challenging, despite extensive research on traditional shape reconstruction over the past decades. At one hand, multi-view stereo [Furukawa et al. 2015] usually assumes a Lambertian-dominant reflectance in computing reliable view-invariant features. Complex appearance variation with view or lighting is not welcome. It may alter the native spatial features on object surface, or specularly reflect the projected pattern from active illumination, either of which may result in correspondence

*: corresponding author

Authors' addresses: Xiang Feng, State Key Lab of CAD&CG, Zhejiang University, China; Kaizhang Kang, State Key Lab of CAD&CG, Zhejiang University, China; Fan Pei, State Key Lab of CAD&CG, Zhejiang University, China; Huakeng Ding, State Key Lab of CAD&CG, Zhejiang University, China; Jinjiang You, State Key Lab of CAD&CG, Zhejiang University, China; Ping Tan, Hong Kong University of Science and Technology, China; Kun Zhou, State Key Lab of CAD&CG, Zhejiang University, China; Hongzhi Wu, State Key Lab of CAD&CG, Zhejiang University, China.

Permission to make digital or hard copies of all or part of this work for personal or classroom use is granted without fee provided that copies are not made or distributed for profit or commercial advantage and that copies bear this notice and the full citation on the first page. Copyrights for components of this work owned by others than ACM must be honored. Abstracting with credit is permitted. To copy otherwise, or republish, to post on servers or to redistribute to lists, requires prior specific permission and/or a fee. Request permissions from permissions@acm.org.

© 2023 Association for Computing Machinery.

0730-0301/2023/8-ART \$15.00

<https://doi.org/10.1145/nnnnnnn.nnnnnnn>

matching errors in shape reconstruction. On the other hand, photometric stereo [Chen et al. 2018; Woodham 1980] takes images captured with fixed view(s) and varying illumination as input. In free-form scanning, however, such images are almost impossible to acquire, as the camera is constantly moving relative to the object.

Recently, image-driven differentiable optimization makes a huge success in geometric reconstruction [Wang et al. 2021; Zeng et al. 2023]. Both the geometry and appearance are optimized simultaneously, with a loss function that encourages the rendering results to approximate corresponding input images in an end-to-end fashion. But for complex appearance such as highly specular or strongly anisotropic reflectance, the result quality is not yet satisfactory, due to the insufficient sampling capability in the illumination domain (e.g., point light) and the insufficient fidelity of appearance representation.

To tackle the above difficulties, our key idea is to employ illumination multiplexing to pack more geometric information into photometric measurements, and subsequently transform them to per-pixel low-level features to enhance 3D reconstruction. In this paper, we present a novel framework to automatically learn to aggregate and transform photometric measurements from multiple unstructured views into spatially distinctive and view-invariant features. The illumination conditions during acquisition and the feature transform are jointly trained on a large amount of synthetic data. Our data-driven framework is highly flexible and can adapt to various factors, including the physical capabilities/characteristics of different setups, and different types of appearance. Since our photometric measurements reveal useful information about appearance as well, we further build a system to scan and reconstruct both the geometry and reflectance for complete object digitization.

The effectiveness of our system is demonstrated on scanning a number of challenging objects with a wide variation of shape and reflectance. Our framework is not tied to any particular setup. We conduct the experiments on a lightweight illumination-multiplexing prototype [Ma et al. 2021], consisting of a camera and an LED array, as well as an off-the-shelf tablet using its front camera and its screen as a programmable light source. Our shape results are validated against reconstructions from a professional 3D scanner, and our appearance results against photographs. We compare favorably with state-of-the-art techniques both in terms of geometry and reflectance.

2 RELATED WORK

Due to the space limit, we only review previous work that is closely related to our approach below. We start with traditional, less end-to-end methods (Sec. 2.1 & 2.2), and then describe latest neural approaches (Sec. 2.3).

2.1 Multi-view Stereo

These methods extract low-level features from each image, compute feature correspondences across multiple views, and apply triangulation to obtain 3D information [Furukawa et al. 2015]. Spatial aggregation is typically needed in feature computation, as the raw measurements at a single pixel are usually not distinctive enough to establish reliable correspondences. While excellent results are

achieved on Lambertian-dominant appearance [Galliani et al. 2015; Schönberger et al. 2016], the reconstruction quality cannot be guaranteed in the presence of complex materials that vary with view and lighting conditions. These material may produce view-varying spatial features that are challenging to match correctly, or reflect the projected spatial patterns in active lighting methods [Levoy et al. 2000; Salvi et al. 2004] away from the camera.

Recently, advances in machine learning are applied to replace hand-crafted features with automatically learned ones [Simonyan et al. 2014; Zagoruyko and Komodakis 2015]. However, computing high-quality features in the presence of complex materials remains difficult, due to the lack of training dataset on physical appearance.

Our work is orthogonal to most techniques here, whose focus is on efficient processing in the spatial domain. In comparison, we focus on how to aggregate useful information in the high-dimensional view-illumination domain for enhanced geometric reconstruction. The optimized lighting patterns essentially serve as convolution kernels to actively probe the *angular* domain. Theoretically speaking, our learned low-level features are modular and can be plugged in any existing multi-view stereo pipeline for subsequent processing.

2.2 Photometric Stereo

These techniques compute a normal field from appearance variations under different illumination conditions and typically at a fixed view, and then integrate the field into a depth map [Shi et al. 2016; Woodham 1980]. Research efforts have been made from the original assumption of a Lambertian reflectance and a calibrated directional light, to more general appearance [Alldrin et al. 2008; Goldman et al. 2009; Shi et al. 2012] and/or uncalibrated lighting conditions [Alldrin et al. 2007; Basri et al. 2007; Lu et al. 2013]. Due to the indirect measurements, the integrated depth results often suffer from low-frequency distortions.

Multi-view photometric stereo leverages photometric cues at multiple views to obtain a complete 3D shape. Starting with an initial coarse geometry, these methods further refine it with the estimated normal information [Hernandez et al. 2008; Li et al. 2020; Zhou et al. 2013]. Vlasic et al. [2009] directly combine multi-view depth maps, each of which computed a corresponding normal field, to produce the final result. Logothetis et al. [2019] exploit the relationship between a signed distance field and normals for reconstruction. The closest work to ours is [Kang et al. 2021]. They learn to probe the angular information with a set of lighting patterns from a fixed view at a time using a light cube, and transform the measurements to useful multi-view feature maps that can be directly used in 3D reconstruction.

All the above work requires taking multiple photographs at a fixed view; none can be applied to free-form scan, in which the camera is constantly moving relative to the physical sample. In comparison, we propose a data structure and network to efficiently aggregate and transform photometric measurements at unstructured views, which are unique to free-form scanning, to low-level geometric features.

2.3 Image-driven Differentiable Optimization

In the past few years, image-driven differentiable optimization of geometry and appearance is developed, using captured images as a

form of self supervision. Various neural scene representations are proposed for the optimization, along with a shading network to account for appearance variations. Representative work includes IDR [Yariv et al. 2020], VolSDF [Yariv et al. 2021] and NeuS [Wang et al. 2021]. While the shading network considerably improves the reconstruction robustness compared with the Lambertian model, the results are not satisfactory with challenging appearance like highly specular materials, due to the difficulty to model them with high fidelity.

A number of techniques [Bi et al. 2020; Luan et al. 2021; Nam et al. 2018; Zhang et al. 2022] focus on recovering detailed geometry and materials using a point light colocated with the camera. While average users can use commodity smartphones/tablets as a scanning device, these methods struggle with objects exhibiting strong specular highlights or anisotropic reflections, due to the extremely low sampling efficiency of a single point light in the angular domain.

Another line of work optimizes geometry and appearance under environment lighting, including NeRFactor [Zhang et al. 2021], NeRV [Srinivasan et al. 2021], NeRD [Boss et al. 2021] and NVD-IFREC [Munkberg et al. 2022]. The material reconstruction of these passive photometric approaches is limited by the frequency distribution of the environment illumination. As a result, the quality of jointly optimized geometry is affected.

Our approach is different from related work in this category. First, we jointly optimize the illumination condition during acquisition to pack more useful information in the measurements for improved reconstruction. The light array we use also has a substantially higher physical sampling capability compared with a flash. Second, we leverage the existing domain knowledge on appearance in training our network, while such knowledge is entirely learned from measurements on a per-object basis in the majority of work on differentiable optimization. Finally, we do not jointly optimize the shape and appearance. This decoupling prevents appearance reconstruction errors from propagating to geometry results [Zeng et al. 2023].

3 ACQUISITION SETUP

We conduct acquisition experiments on two illumination-multiplexing devices, a lightweight custom-built scanner similar to [Ma et al. 2021] (Fig. 1-a) and an off-the-shelf tablet (Fig. 1-b). The intrinsic/extrinsic parameters of the camera, as well as the positions, orientations, angular intensity and spectral distribution of the light sources, are carefully calibrated. We acquire 30/10 images per second on scanner/tablet during scanning, respectively.

Prototype Scanner. Our prototype consists of a rectangular RGB LED array and a single machine vision camera. The LED array has $32 \times 16 = 512$ RGB LEDs, with a pitch of 1cm and a maximum total power of 40W. The intensity of each LED is independently controlled, and quantized with 8 bits per channel for implementation via Power Width Modulation (PWM). A 5MP Basler acA2440-75uc camera is mounted on the top edge of the LED array. A house-made circuit board is in charge of high-precision synchronization between the camera and the LED array.

Tablet. Our tablet is a 12.9-inch iPad Pro (4th gen.). We use its screen as a programmable light source, and employ its front-facing

7MP camera to take photographs. Note that the power of the iPad screen is considerably lower than our scanner, which translates to a higher requirement on hand-held stability to avoid blurred images.

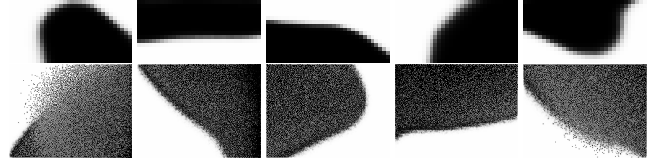


Fig. 2. Learned lighting patterns for acquisition. The top row shows the patterns for our prototype scanner, and the bottom patterns for the tablet.

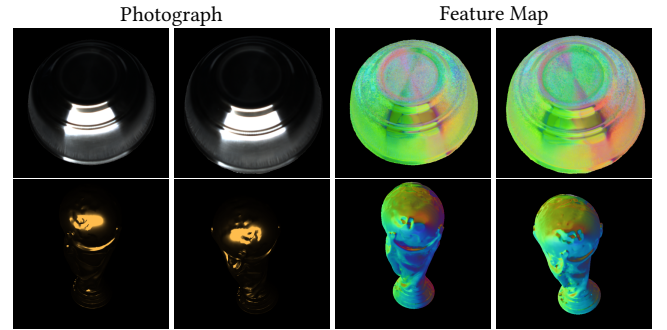


Fig. 3. Visualization of our feature maps at 2 views (3rd/4th column) on a scanned object (top row) and a synthetic one (bottom row). The 1st/2nd column are input photographs at the same view as the 3rd/4th column, respectively. Our high-dimensional features are projected to 3D via PCA for visualization.

4 PRELIMINARIES

The following equation describes the relationship among the image measurement B from a surface point \mathbf{p} , the reflectance f and the intensity I of each LED of the scanner/each pixel of the tablet, the collection of which will be referred to as a **lighting pattern**. Below we focus on a single channel for brevity.

$$B(I, \mathbf{x}_p, \mathbf{n}_p, \mathbf{t}_p) = \sum_l I(l) \int \frac{1}{\|\mathbf{x}_l - \mathbf{x}_p\|^2} \Psi(\mathbf{x}_l, -\omega_l) V(\mathbf{x}_l, \mathbf{x}_p) f(\omega_l'; \omega_o', \mathbf{p}) (\omega_l \cdot \mathbf{n}_p)^+ (-\omega_l \cdot \mathbf{n}_l)^+ d\mathbf{x}_l \quad (1)$$

Here l is the index of a locally planar light source, and $I(l)$ is its intensity in the range of $[0, 1]$, the collection of which will be referred to as a lighting pattern in this paper. Moreover, $\mathbf{x}_p/\mathbf{n}_p/\mathbf{t}_p$ is the position/normal/tangent of \mathbf{p} , while $\mathbf{x}_l/\mathbf{n}_l$ is the position/normal of a point on the light whose index is l . We denote ω_l/ω_o as the lighting/view direction, with $\omega_l = \frac{\mathbf{x}_l - \mathbf{x}_p}{\|\mathbf{x}_l - \mathbf{x}_p\|}$. $\Psi(\mathbf{x}_l, \cdot)$ represents the angular distribution of the light intensity. V is a binary visibility function between \mathbf{x}_l and \mathbf{x}_p . The operator $(\cdot)^+$ computes the dot product between two vectors, and clamps a negative result to zero. $f(\cdot; \omega_o', \mathbf{p})$ is a 2D BRDF slice, which is a function of the lighting direction. We use the anisotropic GGX model [Walter et al. 2007] to represent f .

As B is linear with respect to I (Eq. 1), it can be expressed as the dot product between I and a **lumitexel** c :

$$B(I; \mathbf{p}) = \sum_l I(l) c(l; \mathbf{p})$$

$$c(l; \mathbf{p}) = B(\{I(l) = 1, \forall_{j \neq l} I(j) = 0\}; \mathbf{p}) \quad (2)$$

where c is a function of the light source l , defined on the surface point \mathbf{p} of the sampled object.

5 OVERVIEW

To scan an object, we move an illumination-multiplexing device around to take photographs continuously. The light source on the device is programmed to loop over $\#p$ pre-optimized lighting patterns. The camera exposure is synchronized with the pattern projection.

To reconstruct the geometry, we partition the entire sequence of captured images into groups. Each **group** consists of $\#p$ consecutively captured images/views, with the first one corresponds to the first lighting pattern, etc. Next, for the **center view** of the group (the $\lceil \#p/2 \rceil$ -th image), we aggregate and transform the multi-view photometric information from the entire group of images into a multi-channel map of distinctive and view-invariant features at the same view. The set of all such maps are fed to a modified NeuS [Wang et al. 2021] for 3D reconstruction. To recover the reflectance, we optimize related parameters with respect to input photographs, given the previously reconstructed mesh. The results are stored as texture maps, which can be rendered with any conventional pipeline under novel view and illumination conditions. Please refer to Fig. 4-a for an illustration.

6 OUR NETWORK

The input to our network are $\#p$ patches of lumitexels ($\#p=5$ in all experiments), and each patch is from a view in a group. Together with the lighting patterns, these lumitexels are needed to synthesize image measurements for network training (Sec. 4). Our output is a high-dimensional feature vector at a pixel location in the center view, which coincides with the patch center. The collection of all feature vectors form a feature map. Feature maps from all groups will be sent to a multi-view stereo method for 3D reconstruction. Our network consists 4 parts. Please refer to Fig. 5 for an illustration. Below we describe these parts in order (Sec. 6.1-6.4).

6.1 Linear Encoder

This first part is an encoder, consisting of a linear fc layer. Its weights correspond to the lighting patterns used in acquisition. Its output are 5 image patches of 19×19 , each of which corresponds to a view in a group. The centers of all patches share the same pixel location. Essentially, each element in the output represents an image measurement under a lighting pattern from a particular view, which is modeled as a dot product between a lumitexel and a pattern (Eq. 2).

Note that increasing the patch size would increase the computation cost, while decreasing it would reduce the chance of capturing essential information for transforming to a high-quality feature. The current patch size is determined via multiple experiments.

6.2 Warping

In this part, we warp each of the 5 image patches to a 3D volume called a **measurement volume**, with a resolution of $5 \times 5 \times 128$, to model the 3D uncertainty in the patch. There are 5 measurement volumes corresponding to 5 views in a group.

We first define a measurement volume using the center view. From the center 5×5 region in the patch of the center view, we cast rays from the calibrated camera center towards each pixel in the region. We discretize the ray into 128 different depth hypotheses, uniformly sampled in the range of $[z_{\min}, z_{\max}]$. Each sample represents the center of a voxel in the measurement volume (Fig. 4-b). The depth range $[z_{\min}, z_{\max}]$ is calculated from a coarse bounding box from preprocessing, or can be manually specified. Ideally, a volume of $1 \times 1 \times 128$ is sufficient to model depth uncertainty of the patch center. However, due to inevitable errors in practical estimation of camera poses, we adopt the current resolution to tolerate such inaccuracies.

To fill in the measurement volume of a particular view, we loop over all of its voxels, back project the voxel center to the current image patch, and store the corresponding image measurement along with the acquisition condition to the current voxel. The condition includes (1) one hot-encoding of the lighting pattern index, (2) the pixel location of the current patch in the image, (3) the depth of the current voxel, (4) the camera transform relative to the center view, and (5) the camera pose of the center view. Here we record the acquisition condition, as we want our network to be aware of them, which are related to the final geometric features. Note that the idea of storing acquisition conditions for neural processing is proposed in [Ma et al. 2021] for high-quality appearance scanning. A graphical illustration of the warping process is shown in Fig. 4-b.

6.3 View-Light Aggregation

This part performs the key task of high-dimensional information aggregation, which is critical for efficient processing of free-form scanned data. First, for each iso-depth slice in one measurement volume, we transform it to a lower dimensional latent vector using an autoencoder. As a result, each measurement volume is converted to 128 latent vectors. This step can be viewed as an aggregation along the non-depth spatial dimensions. Next, for each depth, we aggregate across 5 views by performing max pooling on all related latent vectors, and store the result as an intermediate feature. Note that this step aggregates illumination as well, since each view is associated with a different lighting pattern. The output of this part is 128 intermediate features. Now the only dimension that has not been aggregated is the depth, which is left for processing in the next part.

6.4 Feature Transform

This part produces the final geometric feature, which will be fed to a multi-view stereo method for 3D reconstruction. We send all 128 intermediate features to a convolutional neural network to extract a 12D feature as output. This allows the network to automatically learn how to "softly" select the most matching depth (among all 5 views) as well as its corresponding feature.

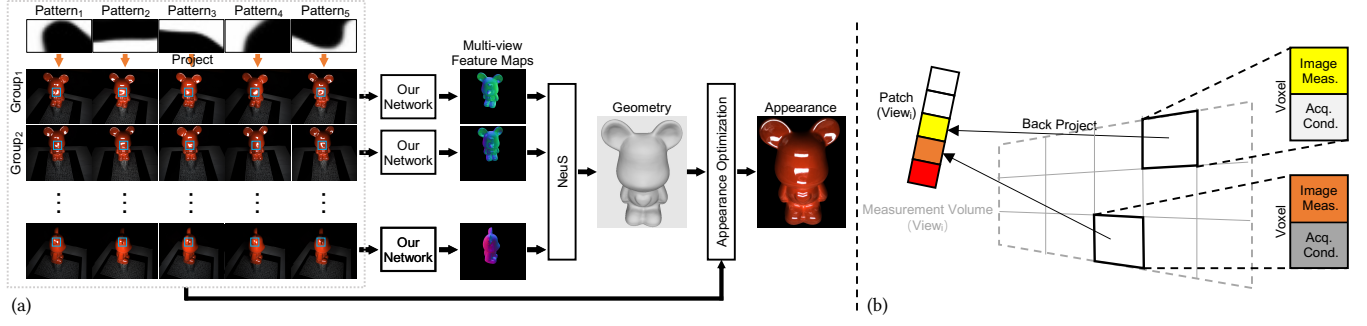


Fig. 4. Our pipeline (a) and warping illustration (b). (a) First, we partition continuously captured images into groups of 5, each acquired under a different lighting pattern. Next, we crop patches from each image in the group, centered at a same pixel location. Our network then transforms these data into a high-dimensional geometric feature at that location, the collection of which forms a feature map at the center view of the group. We feed the feature maps from every group into a multi-view stereo method for 3D reconstruction. With the computed shape, the appearance of the object is differentially optimized with respect to all input images. (b) Here we show a 2D warping example of a patch that belongs to the i -th view in a group. First, a frustum-shaped measurement volume of the i -th view is set up with respect to the center view. We then fill each voxel with an image measurement by back projecting to the patch. The corresponding acquisition condition, including view and lighting information, is also stored.

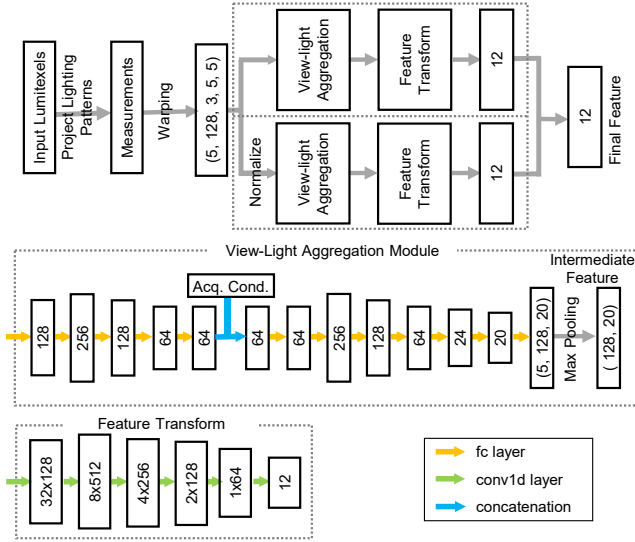


Fig. 5. Network architecture. Our network takes as input the lumitexels corresponding to all pixels in 5 patches from a group, and encodes them as measurements by simulating lighting pattern projections. The measurements of each view are warped to a measurement volume. The total of 5 volumes are aggregated and transformed to a feature vector, by combining the outputs from an unnormalized and a normalized branch that shares the same structure.

The above architecture (Sec. 6.1-6.4) is repeated twice to build two branches. One unnormalized branch works exactly as described above, while the other branch will normalize the volume across multiple views on a per-voxel basis. The idea is to prevent the network from learning stable diffuse albedos only. After normalization, the absolute values of albedos no longer matter, therefore forcing the network to exploit other useful sources of information.

Finally, the two 12D output vectors from both branches are sent to a linear fc layer, to compute a final 12D feature as output, similar to [Kang et al. 2021].

6.5 Loss Function

The loss function is defined as follows:

$$L = \lambda_0 L_0 + \lambda_1 L_1 + \lambda_2 L_2 + \lambda_p L_p,$$

where L_0, L_1, L_2 are the e1 loss on the final feature, feature from the unnormalized/normalized branch, respectively. The e1 loss is a modified version from L2-Net [Tian et al. 2017]:

$$s_{ij}^c = \exp(-d_{ij}) / \sum_m \exp(-d_{mj}),$$

$$s_{ij}^r = \exp(-d_{ij}) / \sum_n \exp(-d_{jn}),$$

$$L_{e1} = \frac{1}{2} \left(\sum_i \log s_{ii}^c + \sum_i \log s_{ii}^r \right).$$

Here d_{ij} is the Euclidean distance matrix of features in a batch of training pairs. We encourage the features of the *same* 3D point at different views to be invariant, and simultaneously increase the distance of features corresponding to *different* points. L_p is a loss term on the brightness of lighting patterns, as brighter patterns are desired for high SNR acquisition during scanning. The definition is:

$$L_p = \max(0, 1 / \sqrt{\sum_l I(l) / \#s - 0.5}).$$

Here $\#s$ is the number of independently controlled light sources. We use $\lambda_0 = 0.33, \lambda_1 = 0.33, \lambda_2 = 0.33$ and $\lambda_p = 0.05$ in our experiments.

6.6 Training

We implement our network with PyTorch, using the Adam optimizer with batch size of 32 and a momentum of 0.9. Xavier initialization is applied to all weights in the network. We train 100K iterations with a learning rate of 10^{-4} , which takes 8 hours to finish.

The training data are synthetically generated using 15 pre-captured objects (Fig. 12) and captured scanning motions. Each object consists of a 3D mesh along with texture maps of GGX BRDF parameters. 25 scanning processes are recorded, each of which consists of 2,000 consecutive camera poses. We compute the relative motion of every 5 views with respect to the center view, which will be processed to synthesize the camera motion for training a single group. Note that our approach is *not tied* to the current data since it is entirely data-driven.

The training/validation data are synthetically generated. We first randomly sample a point on a random object and two visible view directions based on the geometry normal. For each viewing direction, a camera position is randomly generated along the direction within a predefined range of valid distance (16-65cm). Then, for each view, a foreground pixel is randomly selected as the projected position of the point. With the projected pixel and the point position, a camera pose is initialized, and we randomly rotate it around the view direction. Next, two groups of pre-captured continuous scanning motions are randomly picked as the camera poses for all 10 images in the groups. Finally, we prepare the lumitexels for all pixels in related patches, whose center is the projected pixel, in order to synthesize images measurements. We split all data into the training/validation set with a ratio of 8:2.

7 APPEARANCE OPTIMIZATION

After establishing a uv-parameterization over the reconstructed geometry, we compute BRDF parameters at each valid texel via differentiable optimization. For a specific texel, we first project the corresponding 3D position to all visible views to gather its image measurements under learned lighting patterns. We reparameterize the GGX BRDF model plus the local frame with a 16D latent code and jointly train a fully-connected network that transforms the latent code to GGX BRDF parameters and the local frame as in [Xu et al. 2023], by minimizing the difference between rendering results (Eq. 1) and the gathered measurements. Finally, we convert the latent code at each texel to anisotropic GGX BRDF parameters and store them in texture maps as the appearance result.

8 IMPLEMENTATION DETAILS

We remove over-blurry images from our sequence to avoid the negative impact over the final results. We calculate the level of blurriness for each image by [Crété-Roffet et al. 2007], and discard an entire group if the blurriness of any image in the group reaches a threshold.

For each remaining image, we perform structure-from-motion with COLMAP [Schönberger and Frahm 2016] to compute the camera pose from the ARTags [Fiala 2005] placed along with the object. We apply SAM [Kirillov et al. 2023] to segment the object from the background for each center-view image. After geometry reconstruction, a uv-parameterization with a texture resolution of 1024×1024 is generated for appearance optimization (Sec. 7).

For training lighting patterns for iPad, we use a resolution of 150 × 200, which is much lower than the original iPad screen, to save the otherwise prohibitively expensive computational costs.

We modify the original NeuS by changing the output dimension of the last fully-connected layer to 12, the same dimension as our feature vector.

9 RESULTS & DISCUSSIONS

All computation is performed on a server with dual AMD EPYC 7763 CPUs, 768GB DDR4 memory and 8 NVIDIA GeForce RTX 4090 GPUs. All results are rendered with NVIDIA OptiX.

We employ our prototype to scan 4 real objects with complex appearance (BOWL, DOG, BEAR and BIRD). The maximum dimension of each object ranges from 6 to 18 cm. The reconstructed geometry and appearance are shown in Fig. 11 & 13. We also use our iPad to scan BOWL, and Fig. 7 compares the results. The remaining objects are synthetic, and we compute the input images for these objects via physically based rendering with a virtual scanner. It takes about 60 seconds to scan a real object. Please refer to the accompanying video for the scanning process with each device.

For computation, it takes 70 minutes to preprocess the data of an object, including blurriness computation, object segmentation and camera pose estimation. For a group of 5 images, our network needs 20 seconds to transform to a feature map. On average we use 60 groups to reconstruct an object. The geometry reconstruction via NeuS takes 6 hours, while the appearance optimization about 1 hour. Samples of the captured images under our optimized lighting pattern and corresponding feature maps are visualized in Fig. 3.

9.1 Comparisons

In the following comparisons, our approach uses on average 60 groups of images (#images = 300) for reconstructing each object, while competing methods use around 300 images for fairness. In appearance comparisons, we randomly choose 70% of the captured images for training and use the remaining 30% as test images to evaluate novel view and lighting synthesis. The ground-truth geometry of a physical object is obtained with a commercial mobile 3D scanner [Shining3D 2023]. Due to the extreme challenging appearance of our objects, we have to apply fine powder to all surfaces for the scanner to work properly.

Geometry Reconstruction. In Fig. 11, we compare our geometry reconstruction results with other state-of-the-art methods on 5 objects with challenging appearances including specular reflections and textureless regions. The BOWL and DICE also exhibit strong anisotropic appearance. For a fair comparison, both COLMAP and NeuS receive input photographs under environment lighting, as a pilot study shows that using the photographs under our patterns as input results in lower reconstruction quality with their methods. COLMAP and NeuS output unsatisfactory results, due to the complexity of appearance variations. The effectiveness of [Kang et al. 2021] is limited, as it relies on photometric information captured from a fixed view. Our results outperform other methods qualitatively and quantitatively.

Joint Reconstruction of Geometry & Appearance. In Fig. 13, we compare both geometry and appearance reconstructions with related methods. For a fair comparison, IRON [Zhang et al. 2021] takes as input photographs with co-located flash, and NVDIFFREC [Munkberg et al. 2022] captures with environment lighting, as we find that using

the input photographs under our patterns results in lower reconstruction quality reconstructions with their methods. Our approach outperforms competing methods qualitatively, as we can handle challenging appearance by efficiently probing the angular domain with illumination multiplex.

In Fig. 6, we compare with NeRFactor [Zhang et al. 2021] on appearance reconstruction, by rendering the results under novel view and lighting conditions. Their approach relies on precise estimation of the density field, in order to compute visibility, normal, albedo and BRDFs. This estimation may become inaccurate in the presence of complex appearance, leading to unsatisfactory appearance reconstruction, and consequently low-quality rendering results.

We also compare our method with a state-of-the-art image-driven differentiable optimization technique [Zeng et al. 2023] in Fig. 10. Their method struggles to accurately reconstruct the geometry in the presence highly specular reflectance. The end-to-end, joint optimization for shape and appearance is challenging to converge to the correct results in this case. Plus, their point light does not have sufficient sampling capability, leading to an under-constrained optimization.

9.2 Evaluations

In Fig. 14, we evaluate the impact of various factors on reconstructing the geometry of DICE. We first compute the shape with our approach on images rendered with camera motions different from training, as shown in the second image. Next, we evaluate the impact of different lighting patterns. The 3rd/4th image in the figure shows the result computed using our network trained with 5 fixed Gaussian noise patterns/a full-on pattern. The effectiveness of our learned patterns is clear, by comparing the 2nd, 3rd and 4th images. Moreover, we train a network without our warping strategy, which results in considerably higher reconstruction error, as shown in the 5th image. This demonstrates the effectiveness of warping, which efficiently models the 3D uncertainty. The last 2 images evaluate the robustness of our approach against errors in camera pose estimation. We perturb the camera poses with Gaussian noise of different standard deviations as in [Ma et al. 2021], and report the average reprojection errors on top of the 2 images. The 6th image shows that our approach can tolerate a reprojection error of 2 pixels. However, when the error increases to 4, the 3D reconstruction quality degrades as shown in the rightmost image. It is worth noting that the average reprojection error using standard structure from motion (SfM) [Schönberger and Frahm 2016] is 0.6 pixels.

We also test the repeatability of our approach in Fig. 8. Two students, who are not involved in this project, are asked to independently capture about the same number of photographs of the same object with our prototype. The reconstructed shapes are visually similar.

Finally, we demonstrate the modular property of our features, by applying them to boost 3D reconstruction with a different backend, COLMAP. We test on a synthetic object with a homogeneous shiny material. In Fig. 9, we employ COLMAP to reconstruct a 3D shape from images of the object rendered under environment lighting, as well as feature maps computed with our network from the same

number of images under learned lighting patterns. Considerable quality improvement is shown with the help of our learned features.



Fig. 6. Appearance reconstruction rendered with novel environment lighting. The top row are our relighting results, and the bottom row the results from NeRFactor[Zhang et al. 2021], which fails to reconstruct the strong anisotropic reflectance of DICE.

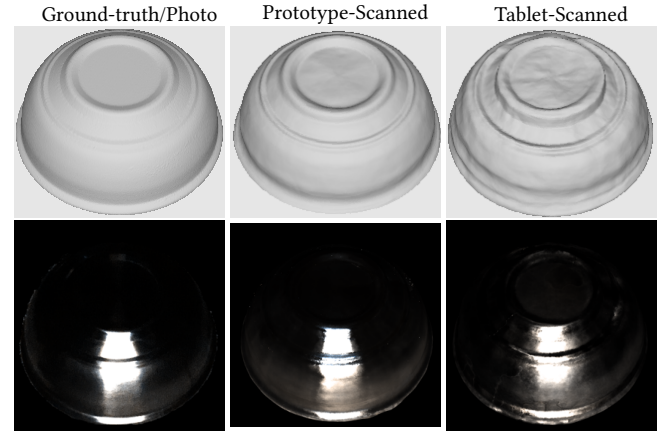


Fig. 7. Comparison of reconstructions of the same object using our prototype and the tablet. The top row shows the shape, and the bottom row rendered appearance with novel view and lighting.

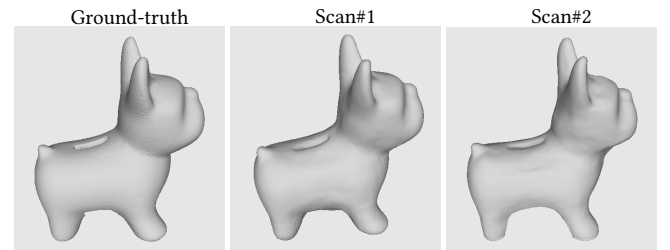


Fig. 8. Repeatability experiment on our geometric reconstruction from 2 scans by 2 different students.

10 LIMITATIONS & FUTURE WORK

Our work is subject to a number of limitations. First, our current imaging pipeline does not account for global illumination effects

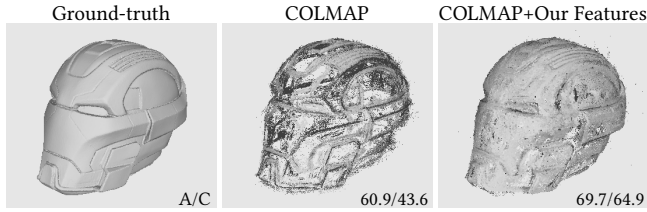


Fig. 9. Boosting another MVS method (COLMAP) with our features. From the left to right: the ground-truth, geometric reconstruction by COLMAP from environment-lit images, and the result by sending our feature maps to COLMAP. Quantitative errors in accuracy/completeness percentage are indicated in the bottom right corner.

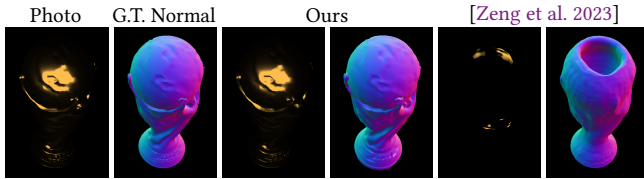


Fig. 10. Comparison between our reconstruction and [Zeng et al. 2023]. For each pair of images, the left one is the appearance rendering, and the right a normal map from the corresponding geometry.

like inter-reflections. Also our system cannot capture transparent/translucent objects, which require special processing. In addition, we need a dark room for high signal-to-noise ratio acquisition, as the uncontrolled environment illumination is not modeled.

It will be interesting future work to address the above limitations. We are also interested in combining our system with a differentiable appearance scanner [Ma et al. 2021], to optimize lighting patterns for the acquisition of both shape and reflectance. Finally, we expect that the reconstruction quality could be further improved, if future tablets could offer APIs that enable hardware synchronization between the camera and screen.

REFERENCES

- Neil Alldrin, Todd Zickler, and David Kriegman. 2008. Photometric stereo with non-parametric and spatially-varying reflectance. In *CVPR*. 1–8.
- Neil G Alldrin, Satya P Mallick, and David J Kriegman. 2007. Resolving the generalized bas-relief ambiguity by entropy minimization. In *CVPR*. 1–7.
- Ronen Basri, David Jacobs, and Ira Kemelmacher. 2007. Photometric stereo with general, unknown lighting. *IJCV* 72, 3 (2007), 239–257.
- Sai Bi, Zexiang Xu, Kalyan Sunkavalli, Miloš Hašan, Yannick Hold-Geoffroy, David Kriegman, and Ravi Ramamoorthi. 2020. Deep reflectance volumes: Relightable reconstructions from multi-view photometric images. In *Computer Vision–ECCV 2020: 16th European Conference, Glasgow, UK, August 23–28, 2020, Proceedings, Part III* 16. Springer, 294–311.
- Mark Boss, Raphael Braun, Varun Jampani, Jonathan T Barron, Ce Liu, and Hendrik Lensch. 2021. NerD: Neural reflectance decomposition from image collections. In *Proceedings of the IEEE/CVF International Conference on Computer Vision*. 12684–12694.
- Guanying Chen, Kai Han, and Kwan-Yee K Wong. 2018. PS-FCN: A flexible learning framework for photometric stereo. In *Proceedings of the European conference on computer vision (ECCV)*. 3–18.
- Frédérique Crété-Roffet, Thierry Dolmiere, Patricia Ladret, and Marina Nicolas. 2007. The blur effect: Perception and estimation with a new no-reference perceptual blur metric. In *SPIE Electronic Imaging Symposium Conf Human Vision and Electronic Imaging*, Vol. 12. EI-6492.
- Mark Fiala. 2005. ARTag, a fiducial marker system using digital techniques. In *2005 IEEE Computer Society Conference on Computer Vision and Pattern Recognition (CVPR'05)*, Vol. 2. IEEE, 590–596.

- Yasutaka Furukawa, Carlos Hernández, et al. 2015. Multi-view stereo: A tutorial. *Foundations and Trends® in Computer Graphics and Vision* 9, 1-2 (2015), 1–148.
- Silvano Galliani, Katrin Lasinger, and Konrad Schindler. 2015. Massively parallel multiview stereopsis by surface normal diffusion. In *ICCV*. 873–881.
- Dan B Goldman, Brian Curless, Aaron Hertzmann, and Steven M Seitz. 2009. Shape and spatially-varying brdfs from photometric stereo. *TPAMI* 32, 6 (2009), 1060–1071.
- Carlos Hernandez, George Vogiatzis, and Roberto Cipolla. 2008. Multiview photometric stereo. *TPAMI* 30, 3 (2008), 548–554.
- Kaizhang Kang, Cihui Xie, Ruisheng Zhu, Xiaohe Ma, Ping Tan, Hongzhi Wu, and Kun Zhou. 2021. Learning Efficient Photometric Feature Transform for Multi-View Stereo. In *Proceedings of the IEEE/CVF International Conference on Computer Vision (ICCV)*. 5956–5965.
- Alexander Kirillov, Eric Mintun, Nikhila Ravi, Hanzi Mao, Chloe Rolland, Laura Gustafson, Tete Xiao, Spencer Whitehead, Alexander C. Berg, Wan-Yen Lo, Piotr Dollár, and Ross Girshick. 2023. Segment Anything. *arXiv:2304.02643* (2023).
- Marc Levoy, Kari Pulli, Brian Curless, Szymon Rusinkiewicz, David Koller, Lucas Pereira, Matt Gintzton, Sean Anderson, James Davis, Jeremy Ginsberg, et al. 2000. The digital Michelangelo project: 3D scanning of large statues. In *Proc. SIGGRAPH*. 131–144.
- Min Li, Zhenglong Zhou, Zhe Wu, Boxin Shi, Changyu Diao, and Ping Tan. 2020. Multi-view photometric stereo: a robust solution and benchmark dataset for spatially varying isotropic materials. *IEEE Transactions on Image Processing* 29 (2020), 4159–4173.
- Fotios Logothetis, Roberto Mecca, and Roberto Cipolla. 2019. A differential volumetric approach to multi-view photometric stereo. In *Proceedings of the IEEE/CVF International Conference on Computer Vision*. 1052–1061.
- Feng Lu, Yasuyuki Matsushita, Imari Sato, Takahiro Okabe, and Yoichi Sato. 2013. Uncalibrated photometric stereo for unknown isotropic reflectances. In *CVPR*. 1490–1497.
- Fujun Luan, Shuang Zhao, Kavita Bala, and Zhao Dong. 2021. Unified shape and svbrdf recovery using differentiable monte carlo rendering. In *Computer Graphics Forum*, Vol. 40. Wiley Online Library, 101–113.
- Xiaohe Ma, Kaizhang Kang, Ruisheng Zhu, Hongzhi Wu, and Kun Zhou. 2021. Free-Form Scanning of Non-Planar Appearance with Neural Trace Photography. *ACM Trans. Graph.* 40, 4, Article 124 (July 2021), 13 pages. <https://doi.org/10.1145/3450626.3459679>
- Jacob Munkberg, Jon Hasselgren, Tianchang Shen, Jun Gao, Wenzheng Chen, Alex Evans, Thomas Müller, and Sanja Fidler. 2022. Extracting triangular 3d models, materials, and lighting from images. In *Proceedings of the IEEE/CVF Conference on Computer Vision and Pattern Recognition*. 8280–8290.
- Giljoo Nam, Joo Ho Lee, Diego Gutierrez, and Min H Kim. 2018. Practical svbrdf acquisition of 3d objects with unstructured flash photography. *ACM Transactions on Graphics (TOG)* 37, 6 (2018), 1–12.
- Joaquim Salvi, Jordi Pages, and Joan Batlle. 2004. Pattern codification strategies in structured light systems. *Pattern recognition* 37, 4 (2004), 827–849.
- Johannes Lutz Schönberger and Jan-Michael Frahm. 2016. Structure-from-Motion Revisited. In *Conference on Computer Vision and Pattern Recognition (CVPR)*.
- Johannes Lutz Schönberger, Enliang Zheng, Marc Pollefeys, and Jan-Michael Frahm. 2016. Pixelwise View Selection for Unstructured Multi-View Stereo. In *ECCV*.
- Boxin Shi, Ping Tan, Yasuyuki Matsushita, and Katsushi Ikeuchi. 2012. Elevation angle from reflectance monotonicity: Photometric stereo for general isotropic reflectances. In *ECCV*. Springer, 455–468.
- Boxin Shi, Zhe Wu, Zhipeng Mo, Dinglong Duan, Sai-Kit Yeung, and Ping Tan. 2016. A benchmark dataset and evaluation for non-Lambertian and uncalibrated photometric stereo. In *CVPR*. 3707–3716.
- Shining3D. 2023. EinScan Pro 2X Plus Handheld Industrial Scanner. <https://www.einscan.com/handheld-3d-scanner/2x-plus/>. [Online; accessed May-2023].
- Karen Simonyan, Andrea Vedaldi, and Andrew Zisserman. 2014. Learning local feature descriptors using convex optimisation. *TPAMI* 36, 8 (2014), 1573–1585.
- Pratul P Srinivasan, Boyang Deng, Xiuming Zhang, Matthew Tancik, Ben Mildenhall, and Jonathan T Barron. 2021. Nerv: Neural reflectance and visibility fields for relighting and view synthesis. In *Proceedings of the IEEE/CVF Conference on Computer Vision and Pattern Recognition*. 7495–7504.
- Yurun Tian, Bin Fan, and Fuchao Wu. 2017. L2-net: Deep learning of discriminative patch descriptor in euclidean space. In *Proceedings of the IEEE conference on computer vision and pattern recognition*. 661–669.
- Daniel Vlasic, Pieter Peers, Ilya Baran, Paul Debevec, Jovan Popović, Szymon Rusinkiewicz, and Wojciech Matusik. 2009. Dynamic shape capture using multi-view photometric stereo. In *ACM SIGGRAPH Asia 2009 Papers*. 1–11.
- Bruce Walter, Stephen R. Marschner, Hongsong Li, and Kenneth E. Torrance. 2007. Microfacet Models for Refraction through Rough Surfaces. In *Rendering Techniques (Proc. EGWR)*.
- Peng Wang, Lingjie Liu, Yuan Liu, Christian Theobalt, Taku Komura, and Wenping Wang. 2021. NeuS: Learning Neural Implicit Surfaces by Volume Rendering for Multi-view Reconstruction. *NeurIPS* (2021).
- Robert J Woodham. 1980. Photometric method for determining surface orientation from multiple images. *Optical engineering* 19, 1 (1980), 191139.

- Xianmin Xu Xu, Lin Yuxin, Haoyang Zhou, Chong Zeng, Yaxin Yu, Kun Zhou, and Hongzhi Wu. 2023. A unified spatial-angular structured light for single-view acquisition of shape and reflectance. In *CVPR*.
- Lior Yariv, Jiatao Gu, Yoni Kasten, and Yaron Lipman. 2021. Volume rendering of neural implicit surfaces. In *Thirty-Fifth Conference on Neural Information Processing Systems*.
- Lior Yariv, Yoni Kasten, Dror Moran, Meirav Galun, Matan Atzmon, Basri Ronen, and Yaron Lipman. 2020. Multiview neural surface reconstruction by disentangling geometry and appearance. *Advances in Neural Information Processing Systems* 33 (2020), 2492–2502.
- Sergey Zagoruyko and Nikos Komodakis. 2015. Learning to compare image patches via convolutional neural networks. In *CVPR*. 4353–4361.
- Chong Zeng, Guojun Chen, Yue Dong, Pieter Peers, Hongzhi Wu, and Xin Tong. 2023. Relighting Neural Radiance Fields with Shadow and Highlight Hints. In *ACM SIG-GRAPH 2023 Conference Proceedings*.
- Kai Zhang, Fujun Luan, Zhengqi Li, and Noah Snavely. 2022. IRON: Inverse Rendering by Optimizing Neural SDFs and Materials from Photometric Images. In *IEEE Conf. Comput. Vis. Pattern Recog.*
- Xiuming Zhang, Pratul P Srinivasan, Boyang Deng, Paul Debevec, William T Freeman, and Jonathan T Barron. 2021. Nerfactor: Neural factorization of shape and reflectance under an unknown illumination. *ACM Transactions on Graphics (TOG)* 40, 6 (2021), 1–18.
- Zhenglong Zhou, Zhe Wu, and Ping Tan. 2013. Multi-view photometric stereo with spatially varying isotropic materials. In *CVPR*. 1482–1489.

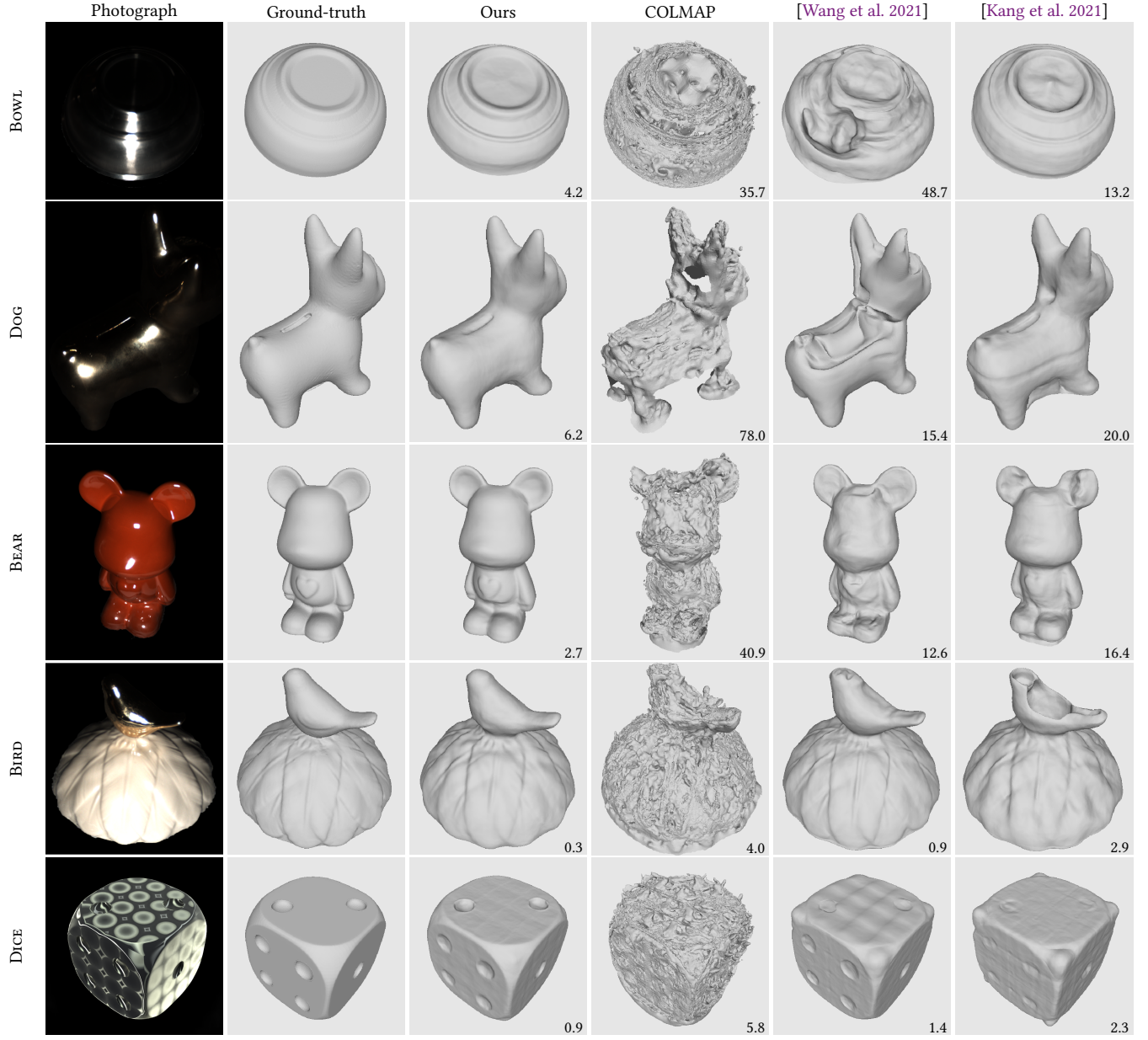


Fig. 11. Comparison with different geometric reconstruction techniques. From the left to right, a photograph, ground-truth geometry, our reconstruction, the result from COLMAP, NeuS [Wang et al. 2021] and EPFT [Kang et al. 2021]. Both NeuS and COLMAP take input photographs under environment lighting. EPFT is re-trained with single learnable lighting pattern to adapt to free-form scanning. BOWL, DOG, BEAR, BIRD are real objects, and DICE a synthetic one. Quantitative errors in Chamfer distance are reported in the bottom-right of related images.

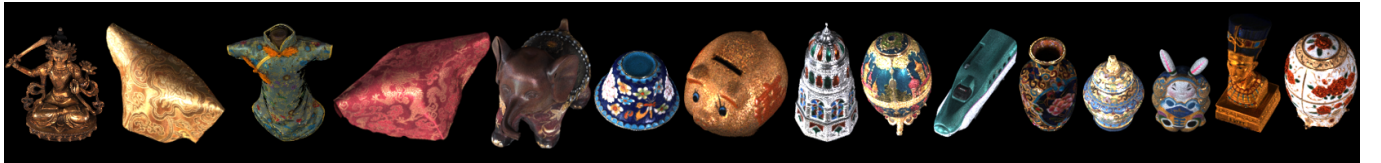


Fig. 12. Our training dataset of 15 high-quality objects, digitized by a commercial 3D scanner and a professional light stage.

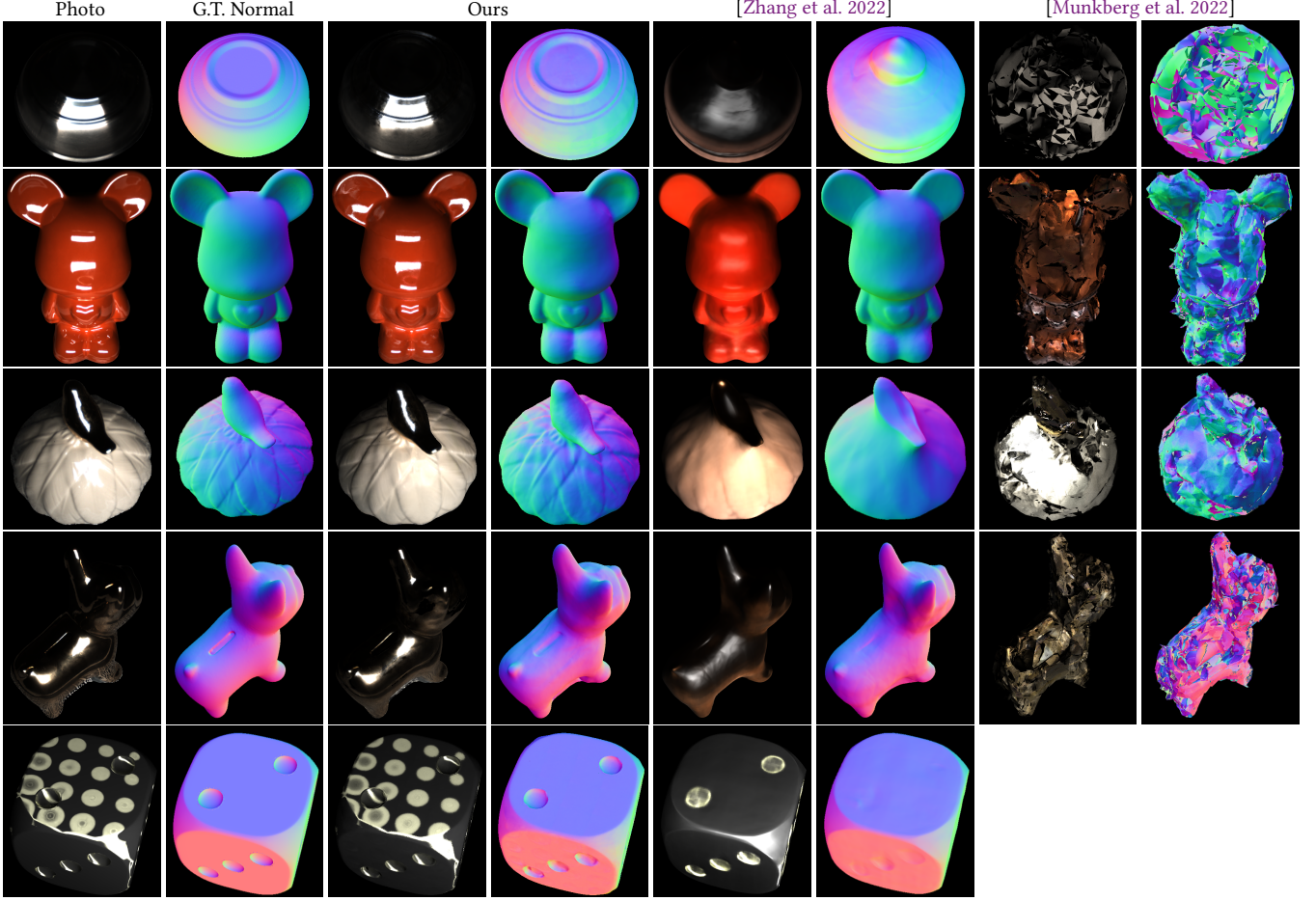


Fig. 13. Comparison with techniques on joint optimization of shape and appearance. For each pair of images, the left one is a photograph/appearance rendered with novel view and lighting, and the right a normal map from the corresponding geometry. From the left to right: ground-truth, our reconstructions, the results from IRON [Zhang et al. 2022] and NVDIFFREC [Munkberg et al. 2022]. The input images are captured with a point light/environment lighting for IRON/NVDIFFREC, respectively. The top 4 rows are real objects, while the last row is synthetic. Note that NVDIFFREC fails to reconstruct Dice due to its strong anisotropic appearance.

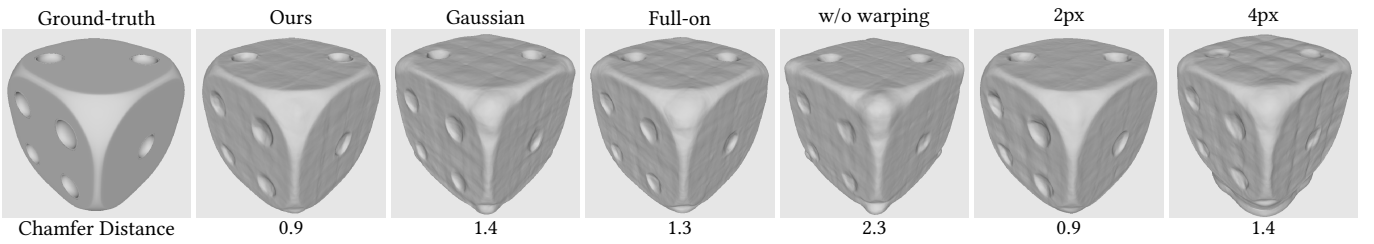


Fig. 14. Impact of different factors over our network. From the left to right: the ground-truth, the reconstruction using our network, ours with 5 Gaussian noise patterns, ours with a full-on pattern, ours without the warping step, and ours with perturbed camera poses (average reprojection error = 2px/4px). Quantitative errors in Chamfer distance are reported at the bottom.